DL-TR-2006-001

CCLRC

An Implicit Algorithm for Capturing Sharp Fluid Interfaces in the Volume of Fluid Advection Method

P.W.Hogg, X.J. Gu *and* **D.R.Emerson**

February 2006

Council for the Central Laboratory of the Research Councils

Enquiries about copyright, reproduction and requests for additional copies of this report should be addressed to:

Library and Information Services
CCLRC Daresbury Laboratory
Daresbury Warrington
Cheshire WA4 4AD
UK
Tel: +44 (0)1925 603397
Fax: +44 (0)1925 603779
Email: library@dl.ac.uk

ISSN 1362-0207

AN IMPLICIT ALGORITHM FOR CAPTURING SHARP FLUID INTERFACES IN THE VOLUME OF FLUID ADVECTION METHOD

P. W. Hogg, X. J. Gu and D. R. Emerson

Department of Computational Science and Engineering
CCLRC Daresbury Laboratory, Warrington, WA4 4AD
United Kingdom
e-mails: p.w.hogg@dl.ac.uk; x.j.gu@dl.ac.uk; d.r.emerson@dl.ac.uk

ABSTRACT

The Volume of Fluid (VOF) method is one of the most effective methods in the simulation of two fluid flows with interfaces where density and viscosity change abruptly. These interfaces are represented implicitly by the values of a colour function which is a volume fraction of one of the fluids. The advantage of the method is its ability to deal with arbitrarily shaped interfaces and to cope with large deformations as well as interface rupture and coalescence in a natural way. In comparison to a Level Set (LS) method, the mass is rigorously conserved in VOF, provided the discretisation is conservative. One of the main difficulties associated with VOF is to advect the interface without diffusing, dispersing, or wrinkling it. This can either be performed algebraically, in schemes such as CICSAM or geometrically, in schemes such as PLIC.

In the present report, an algebraic advection scheme for the interface is presented, which is designed for the implicit time advancing algorithm. Analogous to CICSAM, the new scheme switches smoothly between ULTIMATE-QUICK and the upper bound of the universal limiter, depending on the angle between the interface and the flow direction. Four cases are tested with the present scheme: (i) solid body rotation; (ii) circle in a shear flow; (iii) dam-break and (iv) Rayleigh-Taylor instability. In the first two test cases, prescribed velocity fields are used, thereby allowing the effectiveness of the scheme in advecting the colour function only to be assessed. The scheme is found to outperform six other methods used for comparison in both studies. In solid body rotation simulations a fractional error of 0.19% is calculated in comparison to the next best recorded error of 1.1%. Similarly, in the longest shear flow simulation, a fractional error of 1.2% is calculated in comparison to the next best recorded error of 3.9%. In the final two test cases the advection equation for the colour function is coupled to the Navier-Stokes equations. In dam-break simulations it is found that the resulting solution effectively captures the trends displayed in experimental data for the advancing water front and the residual height of the liquid column against time. Qualitative results obtained for the Rayleigh-Taylor instability modelling in test case four are found to compare favourably to previous numerical simulations of the same phenomenon.

CONTENTS

An Implicit Algorithm for Capturing Sharp Fluid Interfaces in the Volume of Fluid Advection Method

P. W. Hogg, X. J. Gu and D. R. Emerson
Department of Computational Science and Engineering
CCLRC Daresbury Laboratory, Warrington, WA4 4AD
United Kingdom

1 INTRODUCTION

The accurate numerical computation of multi-fluid flows, and the simulation of the flow of two immiscible fluids separated by a well-defined interface, has many applications. One area is that of environmental engineering where it is used to simulate dam and dyke-breaks [1-3], volcanic flows and plumes [4] and the motion of water in a marine environment [5-7]. Another is that of biomedical sciences/engineering, where biological material and fluids such as blood are transported through capillary tubing and channels in the vascular system [8-10] or in Micro Electro Mechanical Systems (MEMS) devices [11-13].

Current numerical methods for simulating such two-phase flows with discrete interfaces can be generally classified as either *interface-tracking (surface) methods* or *interface-capturing (volume) methods* [14]. In *interface-tracking methods* the free surface is treated as a sharp interface whose motion is followed. Some *moving grid techniques* [15] employ a boundary fitted grid, where the grid points are embedded in the fluid and move with it in a Lagrangian manner such that the fluid always coincides with the region to be analysed. Others require the introduction of a *height function* [16], which is the free surface elevation relative to its unperturbed state, whose local change is described though a kinematic boundary condition. The advantage of surface methods is that they maintain a sharp interface for which the exact position is known throughout the calculation. However these methods require special treatment when the interface is subject to large deformation or stretching [17]. In *interface-capturing methods*, the different fluids are marked either by massless particles [18, 19] or by an indicator function, which in turn may be a volume fraction [20, 21] or a level set [22-24]. The advantage of volume methods are in their ability to cope with large stretching and deformation of the interface as well as rupture and coalescence in a natural way. In the massless particle method, individual particles are tracked in a Lagrangian manner across an Eulerian mesh; however such schemes are non-conservative in general. Alternatively, methods which employ an indicator function, solve a scalar transport equation in an Eulerian manner, thereby enabling the enforcement of conservation. The indicator function can either take the form of a scalar step function (known as a colour function) representing the volume fraction of space occupied by one of the fluids (known as VOF), or a smooth but arbitrary function (level set) encompassing a predefined iso-surface which identifies the interface.

One of the main difficulties associated with VOF is advecting the step function without diffusing, dispersing or wrinkling the interface. Various techniques have been proposed for capturing a well-defined interface using volume fractions. These are largely based on either a geometric or algebraic approach. An example of one such method from the first grouping is known as Piecewise Linear Interface Calculation (PLIC) [25, 26]. This relies on an explicit advection of reconstructed line segments. Essentially a predefined set of rules based on the volume fractions of neighbouring cells is used to reconstruct the fluid distribution for a cell. The local velocities move the fluid distributions and the new volume fraction values are updated accordingly. A major problem with such methods is that the cell shapes are implicitly used in the interface reconstruction and so it is very difficult to extend these techniques to arbitrary complex meshes and to three dimensions.

Alternatively an algebraic approach can be adopted in which the convective scalar transport equation for the volume fraction is discretised in such as way so as to guarantee physical (bounded) volume fractions whilst preventing smearing of the interface over several mesh cells. The original VOF scheme [21] was derived as a piecewise constant volume tracking method, with the appealing feature that its volume fluxes can be formulated

algebraically without reconstructing the interface. It takes the interface orientation into account when calculating the amount of fluid fluxed over the face of a control volume, ensures physical volume fraction values (i.e. overall boundedness between zero and unity) and keeps the transitional area over one control volume. However it does not preserve local boundedness i.e. a volume fraction value which initially lies between the values of its neighbours does not necessarily preserve this property when advected in the absence of shear. This numerically introduces new maxima and minima into the volume fraction field and leads to non-physical deformation of the interface shape [27-30].

High resolution differencing schemes such as Total Variation Diminishing (TVD) methods, Flux Corrected Transport (FCT) schemes and techniques using Normalised Variable Diagrams (NVD) [31] offer another approach, but attempts to apply them show that they are too diffusive [32, 33]. Although FCT schemes are non-diffusive by nature they create areas of unphysical flotsam (floating wreckage) or jetsam (jettisoned goods) [28]. Furthermore these schemes are based on one-dimensional derivations with extensions to multi-dimensional flow by operator splitting [34]. This limits their implementation to structured meshes where control volume faces are aligned with the coordinate axes.

In the present report, an algebraic advection scheme for the interface is presented, designed for the implicit time advancing algorithm. The scheme is based on the Compressive Interface Capturing Scheme for Arbitrary Meshes (CICSAM) developed by Ubbink & Issa [35]. This makes use of the NVD concept and switches between different differencing schemes to yield a bounded scalar field, but one which preserves both the smoothness of the interface and its sharp definition (over one or two computational cells).

2 GOVERNING HYDRODYNAMIC EQUATIONS

In the VOF method, one fluid formulation of two-fluid Navier-Stokes equations is employed as the interfacial boundary conditions are implicitly contained in the equation of motion. Both fluids are described by the same set of equations, but the differences in material properties, such as density and viscosity, are explicitly accounted for. Consider two incompressible fluids, 1 and 2, separated by an interface S. The continuity equation is given by

$$\frac{\partial u_i}{\partial x_i} = 0 \tag{1}$$

where u_i is the velocity and x_i is the spatial direction. The flow is governed by the incompressible Navier-Stokes equations:

$$\frac{\partial u_i}{\partial t} + \frac{\partial u_j u_i}{\partial x_j} = -\frac{1}{\rho}\frac{\partial p}{\partial x_i} + \frac{1}{\rho}\frac{\partial \tau_{ij}}{\partial x_j} + \frac{F_i}{\rho} + g_i \tag{2}$$

in which p, g_i and F_i are the pressure, gravity vector and the interfacial surface tension force, respectively and τ_{ij} is the viscous stress tensor given by

$$\tau_{ij} = \mu\left(\frac{\partial u_i}{\partial x_j} + \frac{\partial u_j}{\partial x_i}\right) - \frac{2}{3}\mu\frac{\partial u_k}{\partial x_k}\delta_{ij} \tag{3}$$

where μ is the coefficient of dynamic viscosity and δ_{ij} is the Kronecker delta. The local density, ρ, and viscosity, μ, are defined as

$$\rho = C\rho_1 + (1-C)\rho_2 \quad \text{and} \quad \mu = C\mu_1 + (1-C)\mu_2 \tag{4}$$

where the subscripts denote the different fluids, and C is the volume fraction with a value of unity in fluid 1 and zero in fluid 2. The volume fraction is governed by

$$\frac{\partial C}{\partial t} + u_i \frac{\partial C}{\partial x_i} = 0 \tag{5}$$

The Continuum Surface Force (CSF) model of Brackbill *et al*. [36] has been frequently employed to calculate the surface tension force:

$$F_i = \sigma\kappa \frac{\partial C}{\partial x_i} \tag{6}$$

where σ is the surface tension and κ is the curvature of the interface. The CSF method converts the surface force into a volumetric continuous force, F_i, instead of a boundary condition on the interface. Equations (1)-(5) are discretised using a finite-volume method and an implicit second-order temporal scheme. The pressure and velocity fields are solved on a collocated grid using the SIMPLE [37] algorithm coupled through Rhie and Chow interpolation [38]. Equation (5) is essential for capturing the motion of the fluid interface but accurate discretisation of its step-like behaviour is not straightforward and is the focus for the remainder of the report.

The method of solution operates in an iterative fashion, wherein the equation for the colour function, Eq. (5), is solved first (starting from an initial volume field) and the resultant volume fractions are used to compute the new densities and viscosities throughout the domain according to Eq. (4). The momentum and continuity equations are solved utilising these new values and the process repeats through a number of outer iterations until a suitable convergence criterion has been satisfied, for each time step.

3 Description of the scheme

3.1 Discretisation of the equation

The finite-volume discretisation of the advection equation for the colour function is based on the integral form of Eq. (5) over each control volume and time interval Δt. If P denotes the centre of the control volume (with volume V_P) the first order implicit discretisation gives

$$C_P^{t+\Delta t} = C_P^t - \frac{\Delta t}{V_P} \sum_f (C_f F_f)^{t+\Delta t} \tag{7}$$

where f is the centroid of the cell face and the volumetric flux is given by the term $F_f = \mathbf{A}_f \cdot \mathbf{u}_f$, where $\mathbf{A}$ is the outward-pointing face area vector normal to the face. The summation in Eq. (7) is over all cell faces. In this method, the resultant fluxes are expressed in terms of the unknown colour function values at the new time.

For a cell-centred method, such as that which we will be considering, the cell centre values are used to interpolate the values of the colour function on the faces, C_f, in Eq. (7). Such an interpolation scheme, which should guarantee a bounded solution whilst maintaining the sharpness of the interface, is the focus of this study.

The interpolation of the face values is the same for all faces and it is therefore sufficient to present the derivation for a single face only. Figure 1 contains a schematic representation of a one-dimensional control volume.

Flow Direction

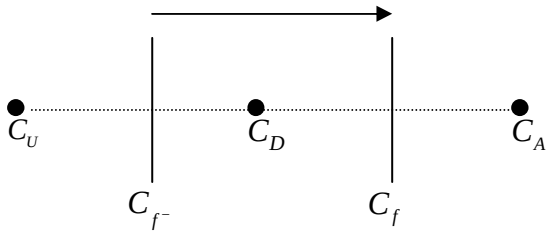

Figure 1. One-dimensional control volume.

The centre cell (donor cell), referred to with subscript D, has two nearest neighbours, referred to with a subscript A for the acceptor cell and a subscript U for the upwind cell. Note that the flow direction determines the location of the neighbours. The face between the donor and acceptor cell, with subscript f, is the face under consideration.

It is reasonable to assume that the interpolated face value will lie somewhere between that of the donor and acceptor cell values. Linear interpolation of the face value, known as central differencing, is second order accurate, but results in an unbounded solution for problems in which convection dominates. The use of the donor cell value (upwind differencing) guarantees a bounded solution but is diffusive and smears the transitional area between the fluids over several cells. The use of the acceptor cell value (downwind differencing) does not preserve boundedness but maintains resolution of the interface. Hence the problem of interface tracking boils down to the selection of a combination of differencing schemes which will preserve both the boundedness of the volume fraction distribution and the sharpness of the interface.

The original VOF scheme, proposed by Hirt & Nichols [21] is a compressive scheme that was developed to capture well-defined interfaces. The amount of volume fraction fluxed over the cell face is calculated by taking account of the volume fractions in both the donor and acceptor cells.

The downwind (acceptor) cell's value is used to maintain (or steepen) the resolution of the interface. Unfortunately, the downwind scheme violates the boundedness criteria, unless used under strictly specified conditions. In order to maintain a bounded volume fraction field, the scheme calculates a blending of the donor and acceptor cell values, and this blended value depends on the availability of the different fluids in the donor cell.

An undesirable feature of the downwind scheme is its tendency to wrinkle the interface when the flow is almost tangential to the interface, for examples see the work of Lafaurie *et al* [29] and Ubbink [30]. To overcome this, the original VOF scheme switched to upwind (donor-cell) differencing when the interface orientation is more likely to be tangential to the flow direction than normal. This switch was activated abruptly as the angle between the interface and the flow direction moved through 45°. An extensive study on the conditions for switching to upwind differencing was conducted in reference [29] and it was found that the accuracy of this methodology is heavily dependent upon this angle. Additionally the work of several authors [27-30] has shown that the original VOF scheme deforms the interface numerically.

An analysis of the formulation by Ubbink [30] has shown that non-physical deformation of the interface originates when employing this methodology because it does not comply with local boundedness criteria and because of the sudden switch between the controlled downwind and upwind differencing schemes.

To overcome this problem Ubbink & Issa [35] proposed that the switch should be between two high-resolution schemes which comply with local boundedness criteria. They argued that a bounded compressive scheme should be used when the interface orientation is more likely to be normal to the flow direction and that a more accurate interpolation scheme, such as bounded central differencing or bounded quadratic upwind interpolation, should be used when the interface is more likely to be tangential to the direction of motion. Furthermore they have demonstrated that the switch between schemes should be more

gradual, rather than the sudden switch proposed by the original VOF scheme. Their mechanism for switching and the high-resolution schemes employed, are described next.

3.2 Normalised Variable Diagram (NVD)

The normalised variable, as proposed by Leonard [31], forms the basis on which the high resolution schemes are constructed and is defined as

$$\tilde{C} = \frac{C - C_U}{C_A - C_U} \tag{8}$$

The normalised variable can be used to give expressions for $\tilde{C}_D$ and $\tilde{C}_f$:

$$\tilde{C}_D = \frac{C_D - C_U}{C_A - C_U} \text{ and } \tilde{C}_f = \frac{C_f - C_U}{C_A - C_U} \tag{9}$$

Gaskell & Lau [39] have presented a convection boundedness criterion (CBC) for one-dimensional implicit flow calculations. The CBC uses the normalised variable and stipulates bounds on $\tilde{C}_f$ for which an implicit differencing scheme in 1D will always preserve the local boundedness criteria:

$$\begin{cases} \tilde{C}_f = \tilde{C}_D & \text{for } \tilde{C}_D < 0 \text{ or } \tilde{C}_D > 1 \\ \tilde{C}_D \le \tilde{C}_f \le 1 & \text{for } 0 \le \tilde{C}_D \le 1 \end{cases} \tag{10}$$

Figure 2 shows the NVD, which plots the normalised face value as a function of the normalised donor-cell value; several common differencing schemes are also shown for comparison. The CBC, as given in Eq. (10) defines the area above and including the line representing upwind differencing in Figure 2 i.e. the upper left triangular area of Figure 2, above and including the diagonal marked UD.

Leonard [31] has shown that various difference schemes and the CBC can be reconstructed for one-dimensional explicit flow calculations using a linear weighting based on the Courant number α, given as

$$\tilde{C}_f = (1 - \alpha)\tilde{C}_f^* + \alpha\tilde{C}_D \tag{11}$$

where $\tilde{C}_f^*$ is the normalised face value for the implicit implementation. With this linearisation $\tilde{C}_f \to \tilde{C}_f^*$ if $\alpha \to 0$ and $\tilde{C}_f \to \tilde{C}_D$ if $\alpha \to 1$; thus a point to point transfer of the upwind nodal value occurs if $\alpha_f = 1$. For explicit flow calculations, the CBC reduces to the universal limiter [31] given by

$$\begin{cases} \tilde{C}_f = \tilde{C}_D & \text{for } \tilde{C}_D < 0 \text{ or } \tilde{C}_D > 1 \\ \tilde{C}_D \le \tilde{C}_f \le \min\left\{1, \dfrac{\tilde{C}_D}{\alpha}\right\} & \text{for } 0 \le \tilde{C}_D \le 1 \end{cases} \tag{12}$$

Figure 3 shows the NVD region for this explicit implementation with an arbitrary Courant number $\alpha = 0.2$.

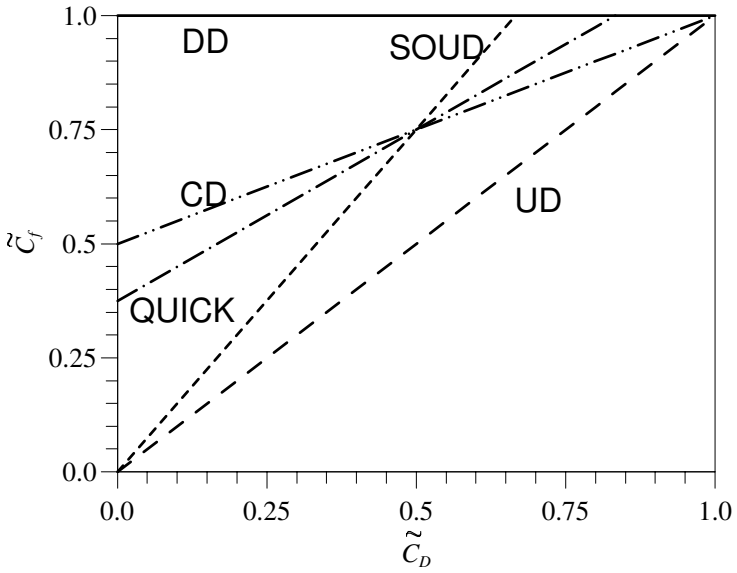

Figure 2. Normalised Variable Diagram (NVD) with the convective boundedness criteria (CBC). UD, Upwind Differencing; CD, Central Differencing; DD, Downwind Differencing; SOUD, Second Order Upwind Differencing; QUICK, Quadratic Upwind Interpolation for Convective Kinematics.

In multi-dimensional flow the worst-case conditions are applied, by defining the Courant number α to be the Courant number of the donor cell, defined as

$$\alpha = \sum_{faces} \left| \alpha_f^{out} \right| \tag{13}$$

where α_f^{out} is the Courant number for each outflow face of the donor cell [30].

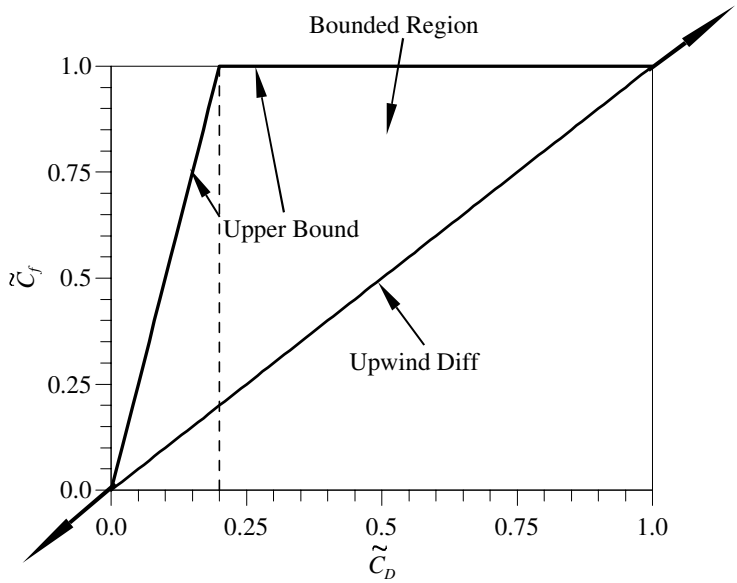

Figure 3. The universal limiter for explicit flow schemes, at an arbitrary Courant number value of 0.2.

A differencing scheme which follows the upper bound of the universal limiter for explicit flow calculations is shown to be very compressive because it turns every finite

gradient in a scalar field into a step profile [31]. Named as HYPER-C by Leonard [31] it is precisely the scheme required when the interface is more likely to be normal to the flow direction.

Although the upper bound of universal limiter as defined in Eq. (12) was derived for explicit schemes it can be seen that its bounded region is merely a subset of the full region defined in Eq. (10) for implicit schemes. The current implicit scheme can therefore utilise this more restrictive criterion, because it guarantees boundedness and provides a compressive scheme to use in appropriate situations where the interface is more normal to the direction of motion.

The universal limiter defined above, together with knowledge gained from the original VOF [21] and reference [29] about taking account of the interface orientation to the direction of motion was applied by Ubbink & Issa to generate CICSAM [35], the basis of the current scheme described in the next section.

3.3 Basis of CICSAM and the current implicit scheme

As has already been stated, the HYPER-C scheme is the most suitable for the advection of a step profile when the interface is normal to the flow direction. The original VOF scheme [21] determines the slope of the interface and switches to upwind differencing if the smallest angle between the interface and the face of the control volume is greater than 45°. An extensive study conducted by Lafaurie *et al* [29], highlighted extensive problems with such an abrupt switching. Ubbink & Issa [35] proposed two main changes. Firstly the scheme should concentrate on how to switch and not when to switch and secondly that some other higher order scheme, other than upwind differencing should be used. Their CICSAM scheme employed ULTIMATE-QUICKEST [31] in this role, but in the spirit of Leonard's ULTIMATE [31] strategy, the current scheme employs ULTIMATE-QUICK, a combination of the universal limiter and QUICK [40]. The mathematical formulation of ULTIMATE-QUICK in the NVD is

$$\tilde{C}_{f_{\text{UQUICK}}} = \begin{cases} \min\left(\dfrac{6\tilde{C}_D + 3}{8}, \tilde{C}_{f_{\text{UL}}}\right) & \text{when } 0 \le \tilde{C}_D \le 1 \\ \tilde{C}_D & \text{when } \tilde{C}_D < 0,\ \tilde{C}_D > 1 \end{cases} \tag{14}$$

Ubbink & Issa [35] defined a weighting factor $0 \le \gamma_f \le 1$ based on the angle between the interface and the direction of motion to calculate the normalised face value. This weighting factor ensures a smooth transition between the upper bound of the universal limiter given by Eq. (12) and the less compressive differencing scheme, represented by ULTIMATE-QUICK, given by Eq. (14). The face value is defined as

$$\tilde{C}_f = \gamma_f \tilde{C}_{f_{\text{UL}}} + \left(1 - \gamma_f\right)\tilde{C}_{f_{\text{UQUICK}}} \tag{15}$$

where $\gamma_f = 1$ is used when the interface is normal to the direction of motion and $\gamma_f = 0$ is used when the interface is tangential to it. As described by Ubbink & Issa [35], this implies that ULTIMTE-QUICK operates where the universal limiter fails to preserve the gradient in the interface and that the universal limiter operates where ULTIMATE-QUICK fails to maintain the sharpness of the interface. The basic derivation of the scheme is complete by stating Ubbink's & Issa's [35] definition of the weighting factor γ_f. This is based on the cosine of the angle θ_f between $(\nabla C)_D$, the vector normal to the interface and the vector $\mathbf{d}_f$ which connects the centres of the donor and acceptor cells and is given by

$$\gamma_f = \min\left(k_\gamma \frac{\cos(2\theta_f)+1}{2}, 1 \right) \tag{16}$$

where

$$\theta_f = \cos^{-1}\left| \frac{(\nabla C)_D \cdot \mathbf{d}_f}{|(\nabla C)_D||\mathbf{d}_f|} \right| \tag{17}$$

and $k_\gamma \geq 0$ is a constant introduced to control the dominance of the different schemes (recommended value of $k_\gamma = 1$). The NVD for the scheme is shown in Figure 4.

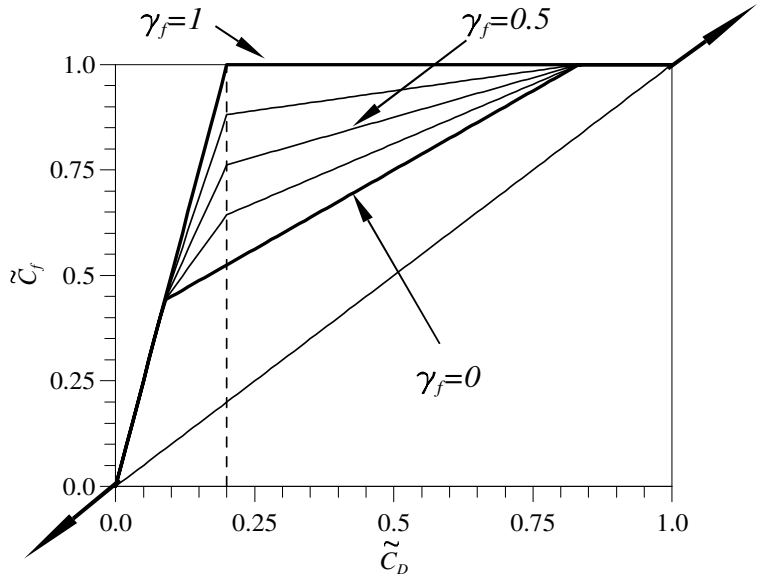

Figure 4. NVD for the Implicit differencing scheme as defined by the universal limiter and ULTIMATE-QUICK.

Although the normalised face value, predicted with the current differencing scheme for one-dimensional uniform flow, in Eq. (15) is important, the actual face value can be derived by algebraic manipulation of Eq. (9) to give

$$C_f = (1-\beta_f)C_D + \beta_f C_A \tag{18}$$

where

$$\beta_f = \frac{\tilde{C}_f - \tilde{C}_D}{1-\tilde{C}_D} \tag{19}$$

The weighting factor β_f, which implicitly contains the upwind value C_U (in the definition of the normalised variables), carries all the information regarding the fluid distribution in the donor, acceptor and upwind cells as well as the interface orientation relative to the direction of motion.

In accordance with CICSAM [35], it can be seen from the NVD in Figure 4 that the formal order of accuracy is not uniform. It varies from first order (upwind or downwind) to second order (centred) to even third order (QUICK) depending on the approximation used for the surface integral over the face.

4 SIMPLE ADVECTION TESTS

Initial problems for the scheme were chosen so as to test the advection of the colour function alone. To this end, analytic velocity fields were used and no attempt was made to couple the advection of C to solutions of the Navier-Stokes equations.

4.1 Simulation of Zalesak's rotating solid body problem

One such test, using a prescribed velocity field, is the "solid body" problem as described by Zalesak [41]. This problem specifically tests the ability of the scheme to translate and rotate a fixed volume, as the fluid region should not deform during the advection.

In this simulation, the motion of a slotted circle with finite boundary was studied in the presence of a unidirectional velocity field at a maximum Courant number of 0.25. The fractional error as a result of the advection of the fraction of fluid was calculated after one full rotation and comparisons were made to the methods implemented in references [28, 35]. The fractional error as a result of the new scheme was found to be approximately an order of magnitude better than those previously obtained. A study of the change in the fractional error against increasing number of rotations was also made and it was found that even after four full rotations the accumulated error was still less than those obtained using the methods tested previously.

4.1.1 Implementation of the rotating solid body simulation

A uniform 2-D square mesh of grid size 200×200 cells was employed to represent a square domain of side 4.0 in length, providing a grid spacing of $\Delta x = \Delta y = 0.02$. A slotted circle was created by removing a slot of width 0.12, from a circle of radius 0.5. This was achieved by removing the section of the circle that lay within 0.06 either side of the vertical downward radial and 0.1 above the circle centre. A finite boundary of half the grid spacing was placed around the entire structure. Initially the fraction of fluid within a cell, $C_{i,j}$ at position (i, j) was set to zero inside the structure and unity outside. Values in the boundary were given by linear interpolation, horizontally for vertical boundaries, vertically for horizontal boundaries and radially at the corners and on the curved edge.

The structure was subject to a unidirectional velocity field, whose components were given by

$$u = -\Omega(y - y_0)\,,\ v = \Omega(x - x_0) \tag{20}$$

where $(x_0, y_0) = (2.0, 2.0)$ is the centre of rotation and where Ω is the angular velocity of 0.5 rads/s, giving a velocity magnitude of 1.0 at the centre of the domain edges. The circle's geometric centre was located at the point $(x, y) = (2.0, 2.75)$. The simulation was integrated forward in time for one full period of rotation, using 2524 time steps each of size $\Delta t = 4\pi/2524$. The fractional error E resulting from the simulation was calculated using

$$E = \frac{\sum_{i,j} \left\| C_{i,j}^{end} - C_{i,j}^{0} \right\|}{\sum_{i,j} C_{i,j}^{0}} \tag{21}$$

where C^{end} is the solution (for the fraction of fluid) at the end of the simulation, C^0 is the initial solution and the summation takes place over all cells at position (i, j). A study of the variation in E against increasing rotation number (effectively increasing time) was made by continuing the simulation for 2, 3 and 4 full rotations, using the parameters already described.

4.1.2 Numerical results

Figures 5(a)-(b) show the shape of the slotted circle at the beginning and end of the simulation for one full rotation. Qualitatively, the results displayed in Figure 5 compare favourably to those obtained by Rudman [28] and Ubbink & Issa [35]. It is found that advecting the discontinuities present at the corners poses the greatest difficulty for the scheme.

The calculated fractional error, as defined in Eq. (21), is displayed in Figure 6(a), together with those obtained for the six other methods described in references [28, 35]. As can be seen from Figure 6(a), the error associated with the present scheme is approximately an order of magnitude less than those previously obtained. This may be attributable to the implicit nature of the present algorithm, which advances the interface with the same up-to-date flow information in all coordinate directions.

The results obtained for the fractional error against increasing time of simulation are displayed in Figure 6(b).

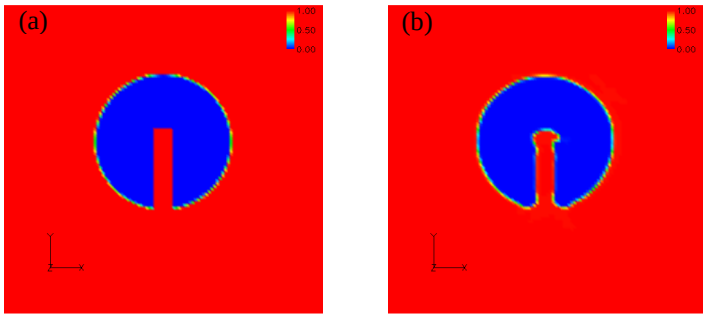

Figure 5. Results for solid body rotation, illustrating the fraction of fluid C through the domain as denoted by the colour scheme in each legend. a) The initial configuration; b) after one full revolution at an angular velocity $\Omega = 0.5$ rads/s.

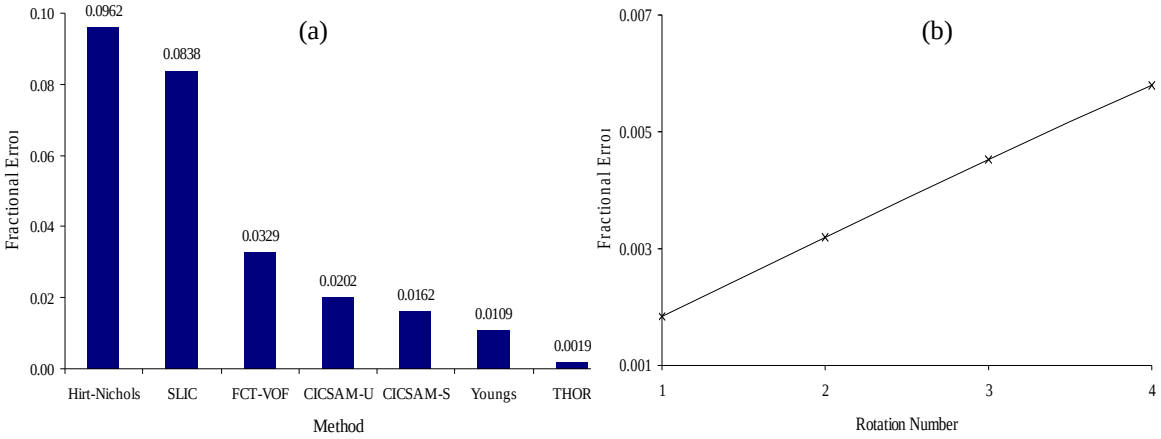

Figure 6. (a) Errors obtained after one full rotation of the slotted circle for the current scheme (THOR) and the six other methods investigated in references [28, 35] and (b) the fractional error measured against time (in units of full rotations).

It can be seen that even after four full rotations, the fractional error accumulated by the present scheme has reached a value of 0.006. This is still lower than the value of 0.0109 that was calculated for the next best scheme (Youngs) after only one rotation. Surface plots of the fraction of fluid after 2, 3 and 4 full rotations are also displayed in Figures 7(a)-(c) for qualitative comparison.

Figure 7 illustrates the increasing deformity undergone by the slotted circle as the rotation number is increased. Those sections of the interface which are located in areas around the corners of the slot have warped and curved, possibly to smooth out the discontinuities that were present at these points. This would also appear to have caused kinks in the curved arc of the interface adjacent to these points. It is not surprising that the calculated fractional error continues to increase with time and Figure 6(b) would indicate that this occurs in a linear fashion.

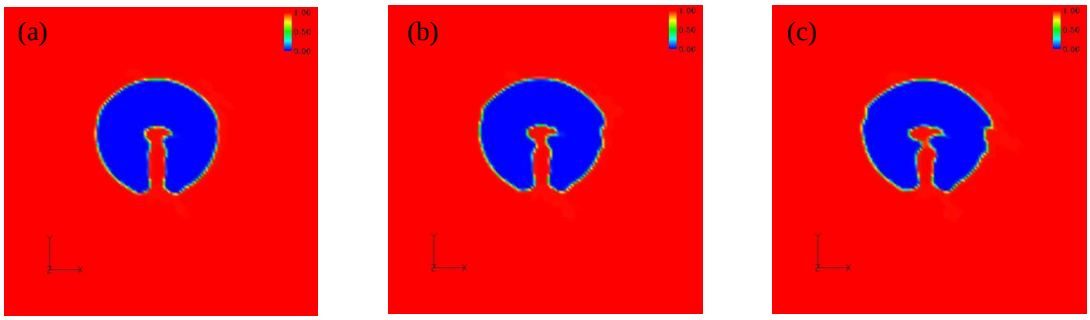

Figure 7. Results for the solid body rotation problem, illustrating the fraction of fluid through the domain, as denoted by the colour scheme in each legend after a) two, b) three and c) four full revolutions at an angular velocity $\Omega = 0.5$ *rads/s.*

4.2 Simulation of the shearing flow problem in two dimensions

An additional and arguably more demanding problem is the shearing flow simulation, as described by Rudman [28] and Ubbink & Issa [35]. The introduction of a shear in the velocity field ensures that topological change occurs as the fluid volume is deformed.

In the problem, the motion of a circle (with finite boundary), in the presence of a shearing velocity field, is studied. The simulation was integrated forward in time for a set number of time steps N, before reversing the sign of the velocity field and integrating for a further N steps in an attempt to return to the initial configuration. Values of N in the range $250 \le N \le 2000$ were tested, with grid spacing and time step size identical to those used in references [28, 35]. The fractional error E was calculated at the end of the simulation and a comparison to the six other numerical schemes studied in references [28, 35] was made. The errors calculated from the present scheme were found to be smaller than those of the six other schemes described. A study of the variation in the fractional error against Courant number was also completed over a number of simulations, each of equal duration.

4.2.1 Experimental procedure for the shearing flow simulation

A square mesh, consisting of 100×100 uniform cells, was used to represent a square domain of side π in length, providing a grid spacing of $\Delta x = \Delta y = \Delta = 0.01\pi$. A circle of radius 0.2π with a finite boundary of width half the grid spacing was centred at position $(0.5\pi, 0.2(1+\pi))$. Initially the fraction of fluid within each cell, $C_{i,j}$ at position (i, j) was set to zero inside the circle and unity outside, with values in the boundary given by linear interpolation in the radial direction. The shearing velocity field was given by components

$$u(x, y) = \cos(x)\sin(y) \ , \quad v(x, y) = -\sin(x)\cos(y) \tag{22}$$

where $|\mathbf{V}|_{\max}$, the maximum magnitude of the velocity field on the domain, has the value of $\sqrt{2}$ in the corners of the domain as both components are unity. Thus at the corners of the domain the requirement is that

$$\Delta t \leq \frac{\sqrt{\Delta x^2 + \Delta y^2}}{|\mathbf{V}|_{\max}} = \frac{\sqrt{2}\Delta}{|\mathbf{V}|_{\max}} \tag{23}$$

This was obtained by enforcing the condition that the speed of information propagation on the domain should not exceed the fluid velocity. Since the maximum Courant number must be less than unity, as would be the case for the explicit schemes described in reference [28], it follows from Eq. (23) that

$$c_{\max} = \frac{|\mathbf{V}|_{\max} \Delta t}{\sqrt{2}\Delta} \tag{24}$$

From the descriptions in references [28, 35], it was clear that a maximum Courant number of 0.25 was used throughout the simulations. Using Eq. (24), a value of $\Delta t = \pi/400$ was calculated and used in order to fairly compare the results. Each simulation ran for N time steps, before reversing the sign of the velocity field and integrating for another N time steps, in an attempt to recover the initial configuration. Values of N in the range $250 \leq N \leq 2000$ were tested.

A study of the effect of the Courant number on the fractional error E, given by Eq. (21), was also completed over simulations of equal duration. In this case a mid-way time of 7.854s was chosen, prior to reversing the sign of the velocity field and integrating for the same period again. The Courant number was varied by changing both the time step and grid spacing and results were obtained in the range $0.25 \leq c_{\max} \leq 1.25$.

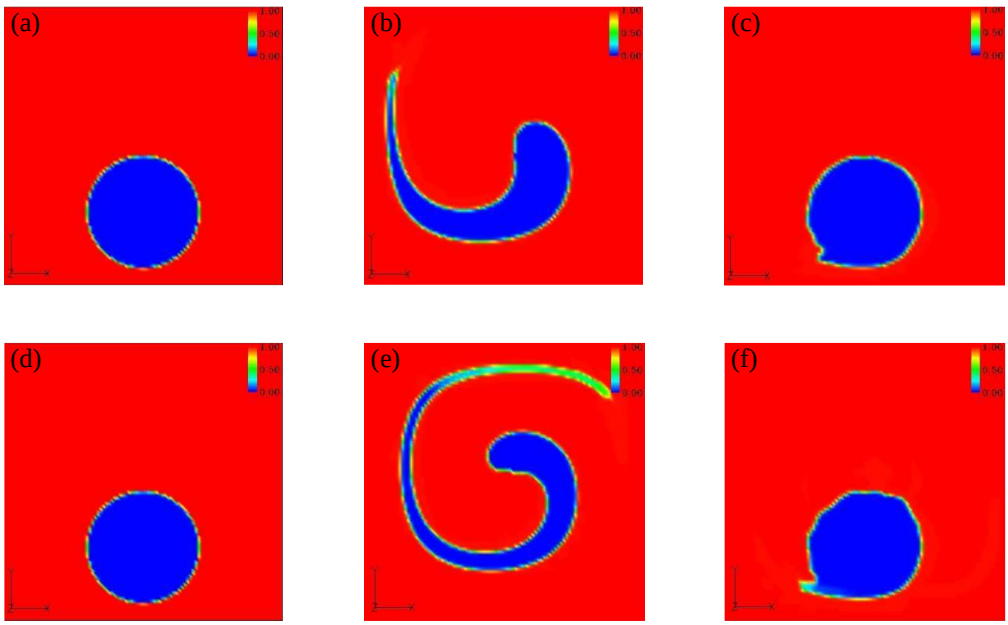

Figure 8. Surface plots of the value of the fraction of fluid for a) initial configuration prior to integration b) after integrating forward 1000 steps c) after integrating back for another 1000 and d) initial configuration prior to integration e) after integrating forward 2000 steps f) after integrating back for another 2000.

4.2.2 Numerical results

Results for the fraction of fluid at three stages during the simulations for $N = 1000$ and $N = 2000$ are shown in Figures 8(a)-(f). The illustrations in Figure 8 compare favourably to those presented in references [28, 35]. It can be seen that as the shearing field stretches the circle, the scheme struggles to capture the tail which is perhaps only 1-2 grid cells in size. The remnants of the tail are clearly visible in the bottom left of the circle in Figures 8(c) & 8(f) and this has an increasingly larger effect on the calculated fractional error as the integration time increases.

Results for the error E after N time steps (forward and back) are shown in Table I for each of the methods described in references [28, 35] and for the current scheme (marked THOR). The same results are displayed graphically in Figure 9 for visual comparison. It can be seen from the calculated errors in Table I and Figure 9 that the current scheme outperforms the results for those given in references [28, 35].

Results for the value of the fractional error E, against maximum Courant number are shown in Figure 10(a). These simulations were performed over a set time, in each case 7.854s. Initially the grid remained unchanged and the time step was systematically increased in order to vary the Courant number, providing the results labelled "Time" in Figure 10(a). After this, a fixed time step was employed and a number of different grids of increasing resolution were employed to vary the Courant number. The results of these simulations are labelled "Space" in Figure 10(a). Note that the Courant numbers quoted are the maximum values found on the domain during that simulation.

Because the maximum Courant number was not felt to be representative of the typical Courant numbers encountered by the circle on the domain, the average Courant number encountered and the standard deviation were calculated for each simulation. The results are shown in Figure 10(b), where a one-to-one correspondence with the points in Figure 10(a) exists.

Figure 10(b) shows that the perception gained by studying errors when considering only maximum Courant numbers can be misleading and that typical Courant numbers encountered by the circle are often much lower than is first thought. This is critically important in the evaluation of the scheme when assessing its likely effectiveness under various conditions.

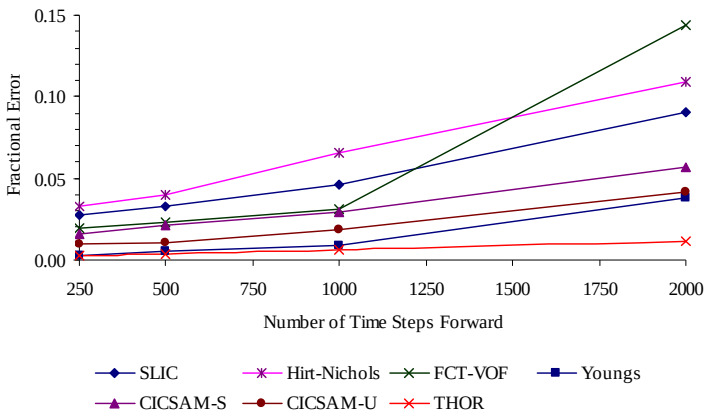

Figure 9. The fractional error E against N for each of the schemes as indicated in the legend.

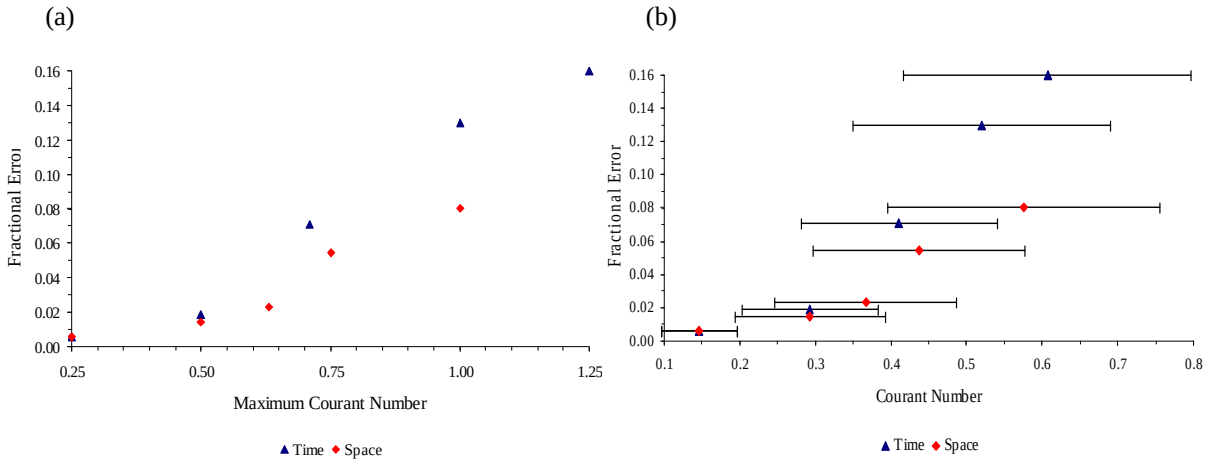

Figure 10. The fractional error against a) maximum Courant number and b) the average Courant number with standard deviation by varying the time step and grid spacing used in the simulation.

5 SIMULATION OF THE COLLAPSE OF A LIQUID COLUMN IN TWO DIMENSIONS

5.1 Overview of the numerical simulation

A number of problems, incorporating coupling of the advection of the colour function with solutions to the momentum equations were then solved. One such problem is the collapse of a liquid column (e.g. a dam-break) for which experimental data is available for comparison. The principle source used in this study was the paper of Martin & Moyce [42], which describes an experimental investigation of this problem and contains experimental measurements. The paper by Kim & Lee [15] also describes a numerical simulation of this problem and was used as an initial starting point to setup the problem and later as a useful reference for comparison.

The separate collapses of two liquid columns in two dimensions were studied. The first was that of a square column of side 0.05715m and the second a rectangular column of height 0.1143m, width 0.05715m. In the case of the square column, the simulation was performed on four separate grids of increasing granularity, using both a fixed time step and a variable time step, but constant maximum Courant number of 0.1. For the rectangular column, the simulation was run on three separate grids of increasing granularity, using both a fixed and variable time step as in the square column case. The numerical integration was carried out over a total simulation time of 0.13s and 0.23s for the square and rectangular columns respectively.

A post-processor was employed to locate the position of the advancing water front and the residual height of the column against time for each case and the results were compared (after rescaling to dimensionless units) to those found by Martin & Moyce [42].

5.2 Experimental procedure

In the first test case, that of the square column, four separate grids were employed and both a fixed and variable time step were used. Table II shows the key spatial and temporal parameters used in each simulation. An additional simulation was also run on each grid. This used a variable time step whose value was recalculated as the simulation progressed in order to maintain a constant maximum Courant number of 0.1.

In the second test case, that of the rectangular column, three separate grids were used and as described above, both a fixed and variable time step were employed. Table III lists the grid and time step parameters used in each simulation.

In both test cases, the liquid column is initially in hydrostatic equilibrium and is "confined" between the left vertical wall of the grid and a notional gate. The fraction of fluid in a cell at position (i, j), represented $C_{i,j}$ is initially set to unity inside the water column, and

zero outside, with a finite boundary of one grid cell being used on the surface. Values for the fraction of fluid inside the boundary are given by linear interpolation in the direction perpendicular to the boundary surface. The gate is suddenly removed at time $t = 0^+$ and the water column starts to collapse under the influence of gravity. Frictionless boundary conditions are specified on the bottom and vertical walls. The density and viscosity of water are taken as 1000 kg/m^3 and 1.0×10^{-3} kgm^{-1}s^{-1} respectively. The ambient fluid is air. Density is taken as 1.0 kg/m^3 and viscosity 1.0×10^{-5} kgm^{-1}s^{-1} respectively. The gravitational acceleration is taken as $g = 9.81$ m/s^2.

5.3 Numerical results

Figure 11 illustrates a typical collapse in time, in this case that of a square column on the 160 x 48 grid using a fixed time step. An interesting feature of the simulation depicted in Figure 11 is the presence of a horizontal jet on the water front. Although these are not visible in photographs of the collapse shown in reference [42], such jets are present in similar experiments performed by Stansby, Chegini & Barnes [1] using modern imaging techniques and equipment. A close up of this feature for the example given in Figure 11 is shown at time $t = 0.13$ s in Figure 12.

Figure 12 illustrates the velocity field profile in the vicinity of the jet. It can be seen that the low volume fraction region on top of the jet appears to be travelling more slowly, as in encounters resistance from the air in the domain. It is likely that this low volume fraction region is a mixed water-droplet/air spray. The effect continues just in front of and above this region where there is a general upward turning in the velocity field as the air is pushed up and over the jet and turns backs.

The position of the water wave front and the height of the residual water column are plotted as functions of elapsed time and compared with experimental data from reference [42]. Figures 13-16 show these plots for the square water column. It should be noted that these simulations correspond to the $a = 2.25$ inch and $n^2 = 1$ experiment of Martin & Moyce [42], where a is the width of the liquid column and n is defined as a constant such that $n^2 a$ is the height of the column. All values have been rescaled to the appropriate dimensionless units described therein.

Horizontally, the distance travelled by the water front from its initial starting point is defined as Z, where $Z = x/a$. Vertically the quantity H represents the residual height, i.e. in comparison to the original starting state. This is defined by $H = y/(n^2 a)$.

Time is defined in two separate units, dependent upon the direction of motion under consideration. Horizontally the unit is T, where $T = nt\sqrt{g/a}$ and vertically τ, where $\tau = t\sqrt{g/a}$.

Figures 13 & 14 show the position of the water front and residual column height against time for the simulations performed using a fixed time step for each of the four grids as described in Table II, whilst Figures 15 & 16 show the position of the water front and residual column height against time, for the simulations run using a variable time step on each of the four grids described in Table II.

It can be seen from Figures 13-16 that there is excellent agreement between the results obtained from numerical simulation and the experimental data. In particular, the general trends followed by the experimental data are clearly modelled in each of the simulations. It can be seen that the results obtained on the two finest grids in each case are very closely matched, indicating that the grid spacing is sufficiently small to have reached a grid independent solution. Conversely it is also clear from the results for the residual column height that the coarsest grid has failed to accurately map the experimental trend in this case. The oscillatory nature of the graph (particularly evident for the 64 x 19 grid results in Figure

14) is due to linear interpolation being used to locate the boundary surface on a very coarse grid.

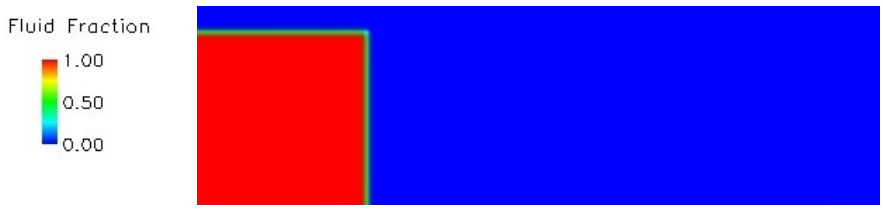

Time t = 0 s

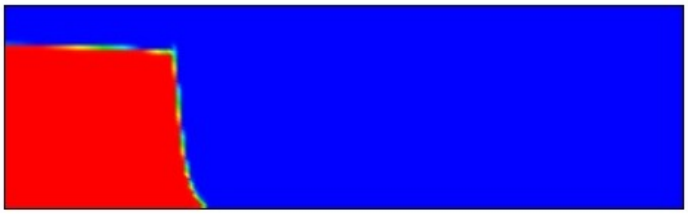

Time t = 0.03 s

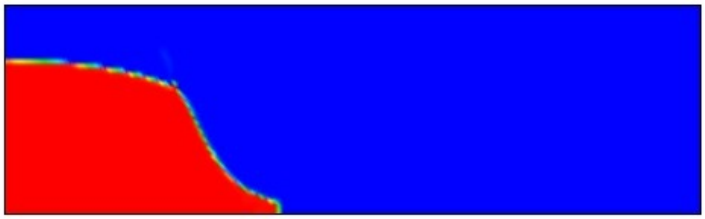

Time t = 0.06 s

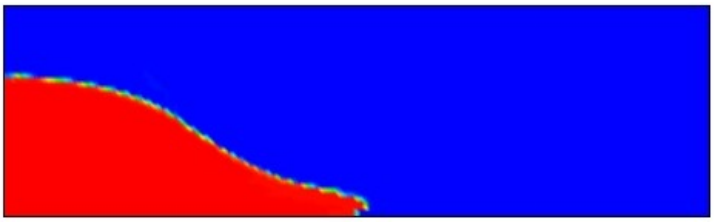

Time t = 0.09 s

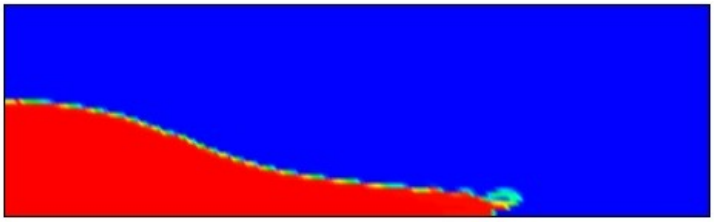

Time t = 0.13 s

Figure 11. The collapse of the square water column on the 160 x 48 grid using a fixed time step at each of the times shown. Each plot shows the fraction of fluid in each cell throughout the domain as given by the spectrum in the attached legend.

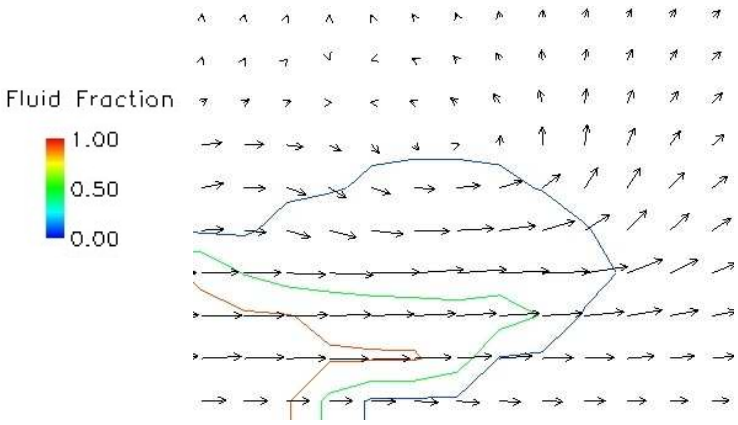

Figure 12. An expanded view of the horizontal jet feature. Velocity vectors are plotted, with relative lengths indicating the magnitude of the velocity at that point on the domain. Contours of 0.1, 0.5 and 0.9 are plotted in the volume fraction field.

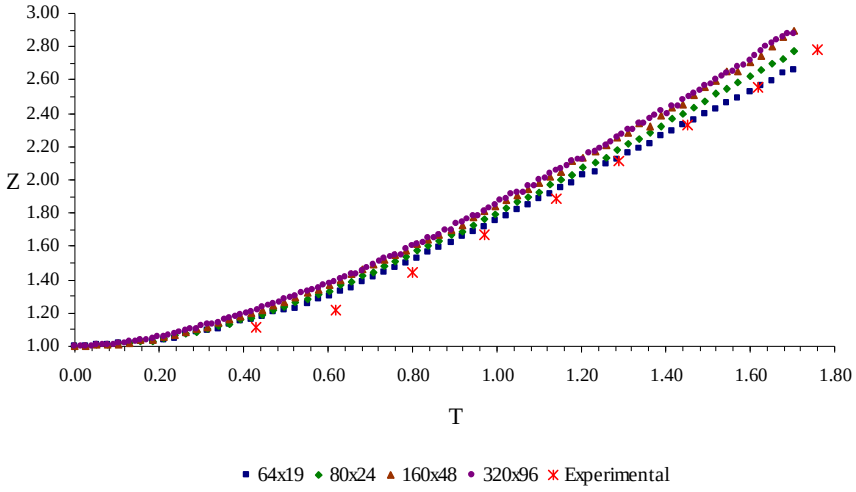

Figure 13. The position of the water front against time for the square column, using a fixed time step.

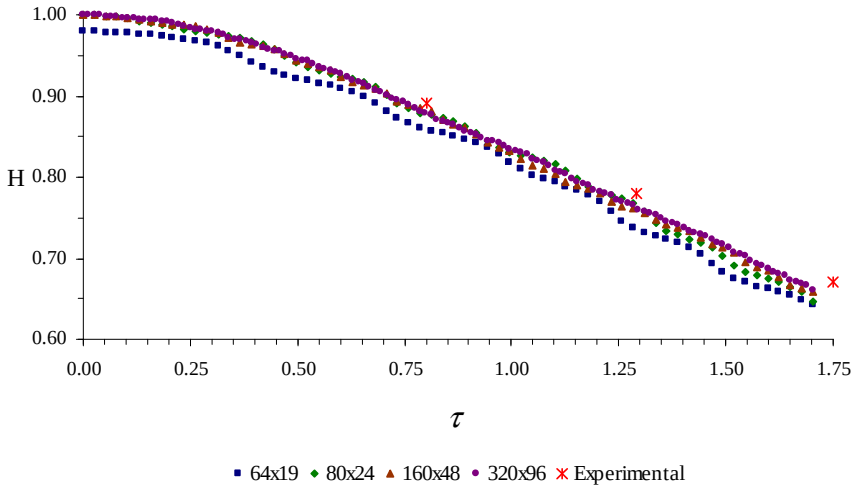

Figure 14. The height of the residual water column against time for the square column using a fixed time step.

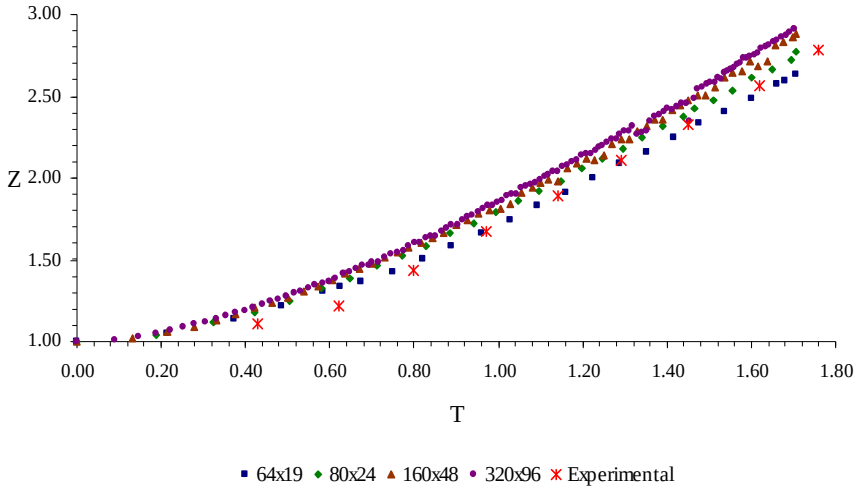

Figure 15. The position of the water front against time for the square column using a variable time step with a fixed maximum Courant number of 0.1.

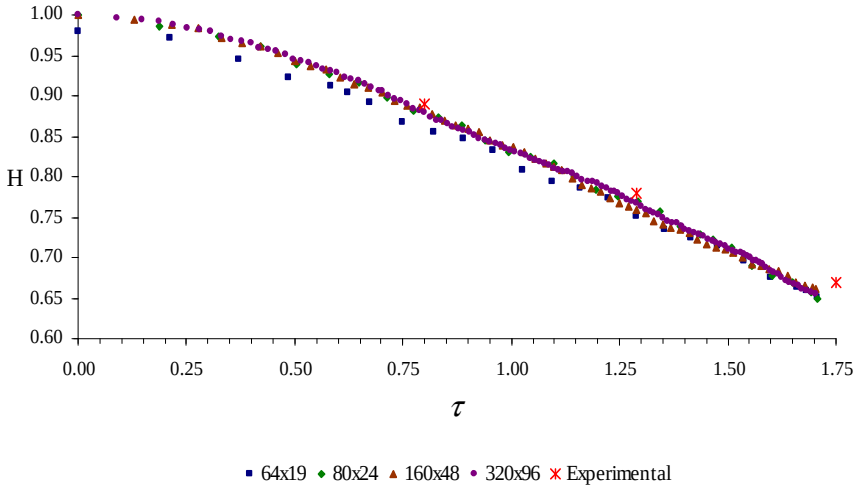

Figure 16. The height of the residual water column against time for the square column using a variable time step and a fixed maximum Courant number of 0.1.

A time lag between the numerical and experimental results, particularly evident in Figures 13 & 15, exists. This may be caused by the fact that experimentally it is very difficult to remove the gate instantaneously and thus there is a finite delay before the column begins to fully collapse. An average value of this delay was calculated by comparing experimental data points 3–8, where the solution is fully developed, to those obtained using the finest grid. The delay was found to be $T = (0.16 \pm 0.01)$ dimensionless units, corresponding to a real time of (12 ± 1) ms.

Figures 17-20 show the same results for the rectangular water column. It should be noted that these correspond to the $n^2 = 2$ and $a = 2.25$ inch experiment of Martin & Moyce [42] with values rescaled to the appropriate dimensionless units as already described.

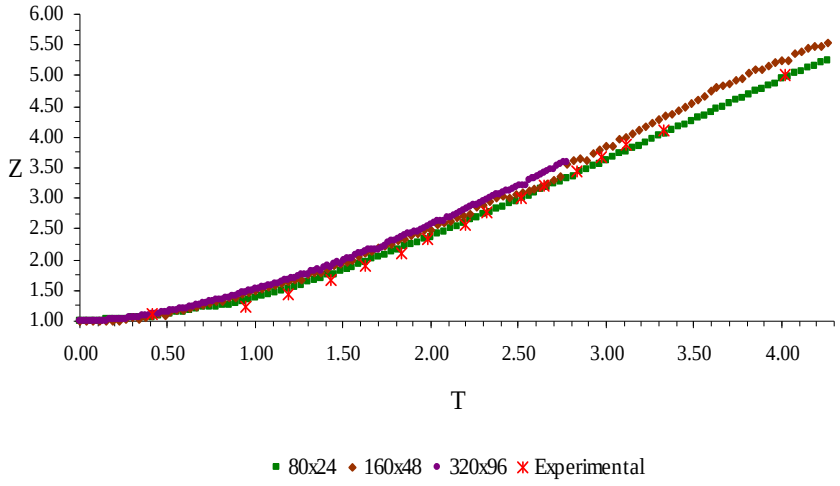

Figure 17. The position of the advancing water front against time for the rectangular column using a fixed time step.

It should also be noted that the shortened graphs for the finest grid in Figures 17-20 are due to insufficient computing time being available to complete the simulations.

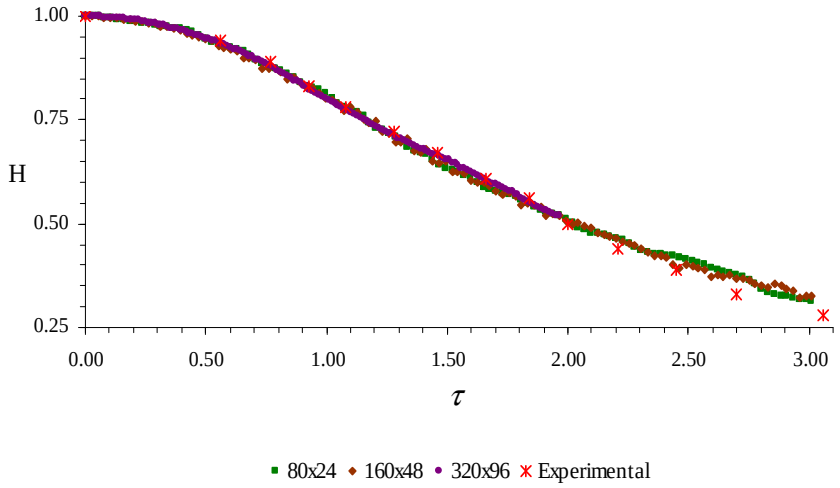

Figure 18. The residual height of the water column against time for the rectangular column using a fixed time step.

Once again the trends displayed in the experimental and numerical data show excellent agreement. As described above, the finite delay between the numerical and experimental data is also clearly visible in these results.

This time an average value for the delay was calculated by comparing experimental data points 4–11 against the solution for the finest grid. The delay was found to be approximately $T = (0.22 \pm 0.02)$ dimensionless units, corresponding to a real time of (12 ± 1) ms, which is identical to that calculated for the square liquid column.

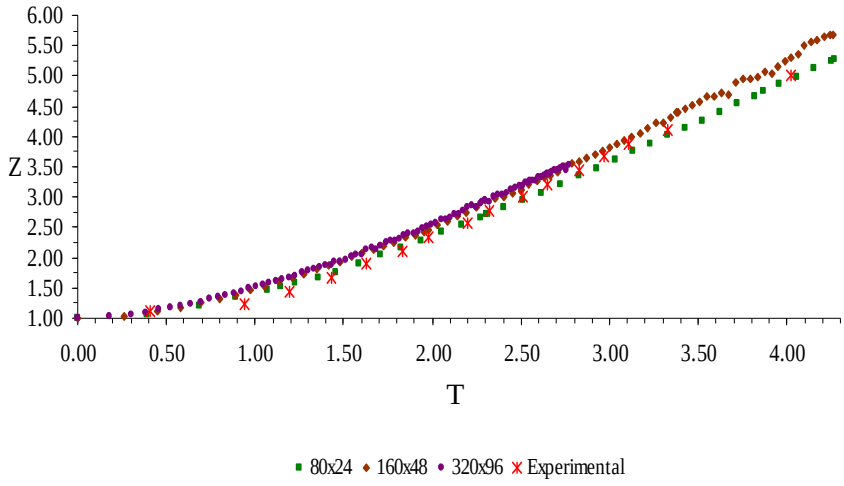

Figure 19. The position of the advancing water front against time for the rectangular water column, using a variable time step and a fixed maximum Courant number of 0.1.

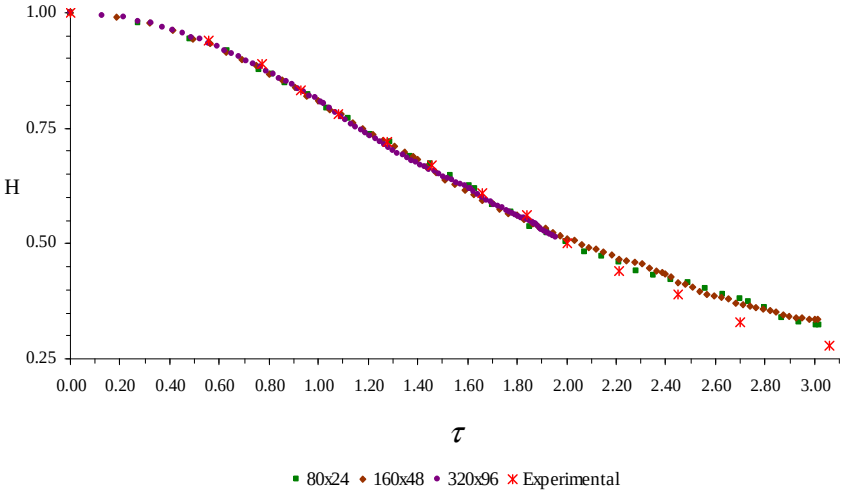

Figure 20. The residual height of the water column against time for the rectangular column, using a variable time step and a fixed maximum Courant number of 0.1.

6 RAYLEIGH-TAYLOR INSTABILITY MODELLING

6.1 Overview of Rayleigh-Taylor instability simulation and experimental procedure

The second problem investigated, involving coupling of the advection equation for the colour function to the Navier-Stokes equations, was that of the Rayleigh-Taylor instability, as presented by López *et al.* [43]. A heavy fluid of density $\rho_1 = 1.225$ kg/m^3 is placed above a lighter fluid of density $\rho_2 = 0.1694$ kg/m^3 in a rectangular domain 1m wide by 4m high. The viscosity of both fluids was taken as 3.13×10^{-3} kgm^{-1}s^{-1}. Due to the symmetry of the problem, only half of the physical domain was solved. This was represented by a grid of 32 x 256 cells in the horizontal and vertical directions respectively, giving a grid spacing of and $\Delta x = \Delta y = \Delta = 0.015625$ m. The integration was performed using a variable time step, but constant maximum Courant number of 0.1 in the domain, in order to reduce computing time. Free slip boundary conditions were imposed at both the upper and bottom

boundaries, with both lateral boundaries having symmetry conditions imposed upon them. The interface shape was initially given by the cosine function $y = -0.05\cos(2\pi x)$.

6.2 Numerical results for Rayleigh-Taylor instability modelling

Figure 21 shows the progression of the Rayleigh-Taylor instability simulation with time. As can be seen in Figure 21, the results are qualitatively comparable to those in reference [43] and the general form of the nonlinear dispersion of the more dense material, displays a similar pattern. Particular points of similarity are the downward vertical plume at the right edge of the domain, the upward hook emanating from the left edge of this plume and its tapering through a fine connecting filament to a larger blob of material. The main difference between the two results are in the presence of another kink in the interface, that has developed just above the initial starting position at time $t = 0.95$ s. In the simulation of López *et al* [43], the interface drops smoothly downward from its position on the high left to the downward plume on the right side of the domain. These discrepancies are due to the different natures of both schemes and are probably dependent upon how compressive or diffusive the scheme is in its treatment of the interface.

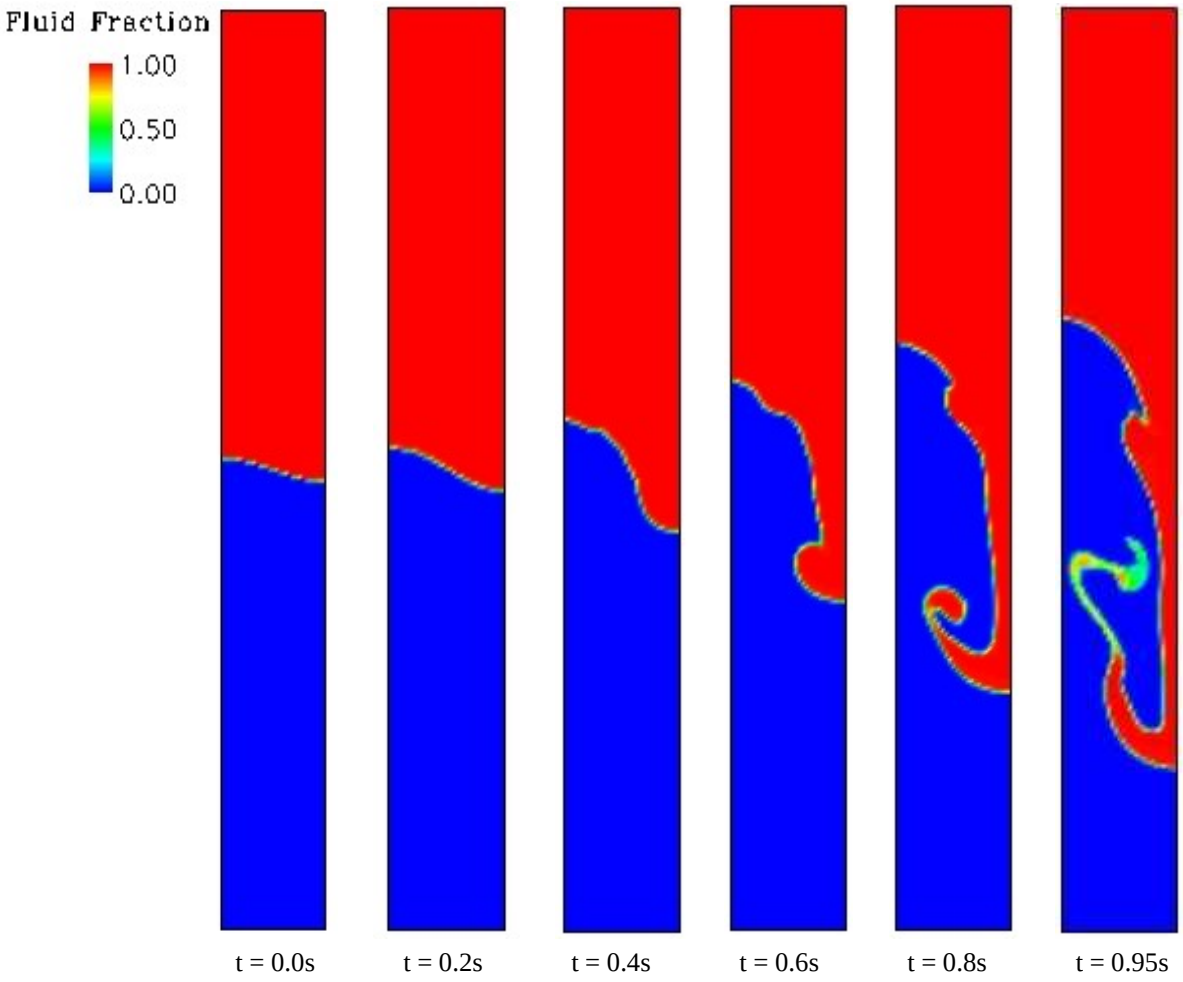

Figure 21. Illustration of the progression of the Rayleigh-Taylor instability with time as given by the fraction of fluid across the domain at each of the times shown.

7 CONCLUDING REMARKS

In general it has been seen that the Volume of Fluid (VOF) method [21] solves a convective scalar transport equation for a colour function, representing the fraction of a fluid in each cell throughout the computational domain. Such an equation is coupled to the momentum equations through expressions for the local density and viscosity in each cell due to the relative quantities of both fluids. An algebraic approach to solving this problem is to discretise the equation in such a manner so as to maintain both the boundedness of the volume fraction and the resolution of the interface.

The scheme introduced in this report is based on the Compressive Interface Capturing scheme for Arbitrary Meshes (CICSAM) of Ubbink & Issa [35]. The scheme switches smoothly between the upper bound of the universal limiter [31] and ULTIMATE-QUICK, a combination of the universal limiter and QUICK [40], dependent upon the angle between the interface and the direction of motion. The scheme has been implemented in the implicit time advancing algorithm, in conjunction with an in-house Navier-Stokes solver developed by the Computational Engineering Group at Daresbury Laboratory.

Numerical results for four main test cases have been presented. In the first two cases, prescribed velocity fields were used and coupling to the Navier-Stokes equations did not occur, in order to enable direct testing of the scheme. Test one assessed the ability of the scheme to simulate Zalesak's solid body of rotation problem and the second its ability to simulate the motion of a fluid volume in a shearing velocity field. In both tests the current scheme outperformed six other methods tested by Rudman [28] and Ubbink & Issa [35] for comparison.

In the final test cases, the advection equation for the volume fraction was coupled to the Navier-Stokes equations and two real fluid flow problems were examined. Test case three examined the collapse of liquid columns under gravity, representing various dam-breaks. It was found that simulation data for the position of the advancing water front and for the residual height of the column against time, accurately modelled that presented in an experimental investigation by Martin & Moyce [42]. Additionally, qualitative results for the nature of the flow during the dam-break indicated the presence of horizontal jets above the boundary, an effect observed in an experimental investigation by Stansby, Chegini & Barnes [1]. In the final test case, a Rayleigh-Taylor instability problem was investigated and the qualitative results obtained agreed with those observed in numerical simulations by López *et al* [43].

8 ACKNOWLEDGEMENTS

Thanks are given to Drs R. W. Barber and Y. H. Zhang for their useful discussions. Thanks also are given to EPSRC for their support to develop the code THOR-VOF through CCP12.

9 LIST OF TABLES

Table I. Results for the fractional error obtained after integrating a total of N steps forward, followed by N steps back for each numerical scheme.

	Scheme Used for Integration						
N	**SLIC [28]**	**Hirt-Nichols [28]**	**FCT-VOF [28]**	**Youngs [28]**	**CICSAM-S [35]**	**CICSAM-U [35]**	**THOR**
250	2.72×10^{-2}	3.24×10^{-2}	1.94×10^{-2}	2.61×10^{-3}	1.63×10^{-2}	9.39×10^{-3}	2.27×10^{-3}
500	3.30×10^{-2}	4.00×10^{-2}	2.35×10^{-2}	5.12×10^{-3}	2.09×10^{-2}	1.10×10^{-2}	3.46×10^{-3}
1000	4.59×10^{-2}	6.60×10^{-2}	3.14×10^{-2}	8.60×10^{-3}	2.90×10^{-2}	1.82×10^{-2}	5.95×10^{-3}
2000	9.02×10^{-2}	1.09×10^{-1}	1.44×10^{-1}	3.85×10^{-2}	5.67×10^{-2}	4.17×10^{-2}	1.17×10^{-2}

Note: Data is taken from the relevant reference as indicated.

Table II. The parameters used in each of the simulations for the square liquid column.

Physical Grid Size, horizontally and vertically (m)	**Grid Size in units of Column Height , H, horizontally and vertically**	**Cells used in the horizontal (x) and vertical (y) directions**	**Horizontal Grid Step Δx (m)**	**Vertical Grid Step Δy (m)**	**Time Step, when used Δt (s)**
0.2286 x 0.06858	4H x 1.2H	64 x 19	3.57×10^{-3}	3.61×10^{-3}	2.0×10^{-4}
0.2286 x 0.06858	4H x 1.2H	80 x 24	2.86×10^{-3}	2.86×10^{-3}	2.0×10^{-4}
0.2286 x 0.06858	4H x 1.2H	160 x 48	1.43×10^{-3}	1.43×10^{-3}	1.0×10^{-4}
0.2286 x 0.06858	4H x 1.2H	320 x 96	7.14×10^{-4}	7.14×10^{-4}	1.0×10^{-4}

Note: All dimensions are described horizontally and then vertically and that four additional simulations employing the same grid parameters but variable time steps were also completed.

Table III. The parameters used in each of the simulations for the rectangular liquid column.

Physical Grid Size, horizontally and vertically (m)	**Grid Size in units of Column Height , H, horizontally and vertically**	**Cells used in the horizontal (x) and vertical (y) directions**	**Horizontal Grid Size Δx (m)**	**Vertical Grid Size Δy (m)**	**Time Step, when used Δt (s)**
0.4572 x 0.13716	4H x 1.2H	80 x 24	5.72×10^{-3}	5.72×10^{-3}	2.0×10^{-4}
0.4572 x 0.13716	4H x 1.2H	160 x 48	2.86×10^{-3}	2.86×10^{-3}	2.0×10^{-4}
0.4572 x 0.13716	4H x 1.2H	320 x 96	1.43×10^{-3}	1.43×10^{-3}	1.0×10^{-4}

Note: All dimensions are described horizontally and then vertically and that four additional simulations employing the same grid parameters but variable time steps were also completed.

10 REFERENCES

1. P. K. Stansby, A. Chegini and T. C. D. Barnes, "The initial stages of dam-break flow", *J. Fluid Mech.* Vol. **374**, pp. 407-424 (1998).
2. S. Muzaferija and M. Perić, "Computation of free surface flows using interface-tracking and interface-capturing methods", In O. Mahrenholtz and M. Markiewicz (eds), *Nonlinear Water Wave Interactions*, Chap. 2, pp. 59-100 (1999).
3. Q. Liang, A. G. L. Borthwick and G. Stelling, "Simulation of dam- and dyke-break hydrodynamics on dynamically adaptive quadtree grids", *Int. J. Numer. Meth. Fluids*, Vol. **46**, pp. 127-162 (2004).
4. M. Pelanti and R. J. LeVeque, "High-Resolution Finite Volume Methods for Dusty Gas, Jets and Plumes", submitted to *SIAM J. Sci. Comput. 15th Jan 06.* Available from http://www.amath.washington.edu/~rjl/pubs/dustyjet/index.html.
5. R. Azcueta, "Computation of turbulent free-surface flows around ships and floating bodies", PhD Thesis, Technical University of Hamburg-Harburg, Germany.
6. S. Muzaferija, S. Perić, M. Sames and T. Shellin, "A two-fluid Navier-Stokes solver to simulate water entry", *Proc. 22nd Symposium on Naval Hydrodynamics*, Washington D.C. (1998).
7. I. Hadžić, F. Mallon and M. Perić, "Numerical simulation of sloshing", *Proc. Workshop on Numerical Simulation of Two-Phase Flows*, Ship Research Institute, Tokyo, pp. 45-57 (2001).
8. D. N. Ku, "Blood flow in arteries", *Ann. Rev. Fluid Mech.* Vol. **29**, pp. 399-434 (1997).
9. G. Abdoulaev, S. Cadeddu, G. Delussu, M. Donizelli, L. Formaggia, A. Giachetti, E. Gobbetti, A. Leone, C. Manzi, P. Pili, A. Scheinine, M. Tuveri, A. Varone, A. Veneziani, G. Zanetti and A. Zorcolo, "ViVa: The Virtual Vascular project", *IEEE Transactions on Information Technology in Biomedicine*, Vol. **2**, No. 4, pp. 268-274 (1998).
10. O. E. Jensen, "Physiological Fluid Dynamics", *In Mathematical and Computational Modelling of Biological Systems*, J. A. C. Martins and E. A. C. Borges (eds), Pires, Centro Internacional de Matemática, Lisbon, Portugal (2003).
11. K. Gabriel, J. Jarvis and W. Trimmer (eds), "Small machines, Large Opportunities: A report on the emerging field of microdynamics", National Science Foundation, AT&T Bell Laboratories, Murray Hill, New Jersey, USA (1988).
12. M. Gad-el-Hak, "The fluid mechanics of microdevices – The Freeman Scholar Lecture", *J. of Fluids Engineering*, Vol. **121**, pp. 5-33 (1999).
13. J. Knight, "Honey I shrank the lab", *Nature (London)*, Vol. **418**, pp. 474-475 (2002).
14. J. H. Ferziger and M. Perić, "Computational Methods for Fluid Dynamics", *Springer-Verlag, Heidelberg* (1996).
15. M. S. Kim and W. I. Lee, "A new VOF-based numerical scheme for the simulation of fluid flow with free surface. Part I: New free surface-tracking algorithm and its verification", *Int. J. Numer. Meth. Fluids.* Vol. **42**, pp. 765-790 (2003).
16. L. Thé, G. D. Raithby and G. D. Stubley, "Surface-adaptive finite-volume method for solving free-surface flows", *Numer. Heat Transfer, Part B*, Vol. **26**, pp. 367-380 (1994).
17. S. O. Unverdi and G. Tryggvason. "A Front Tracking Method for Viscous, Incompressible, Multi-Fluid Flows", *J. Comput. Phys.* Vol. **100**, pp. 25-37 (1992).
18. F. H. Harlow and J. E. Welch, "Numerical Calculation of Time-Dependent Viscous Incompressible Flow of Fluid with Free Surface", *Phys. Fluids.* Vol. **8**, pp. 2182-2189 (1965).
19. B. J. Daly, "Numerical Study of Two Fluid Rayleigh-Taylor Instability", *Phys. Fluids.* Vol. **10**, pp. 297-307 (1967).
20. W. F. Noah and P. Woodward, "SLIC (Simple Line Interface Calculation)", *Lect. Notes in Phys*, Vol. **59**, *Proceeding of the Fifth International Conference on Numerical Methods in Fluid Dynamics*, pp. 330-340 (1976).
21. C. W. Hirt and B. D. Nichols, "Volume of Fluid (VOF) Method for the Dynamics of Free Boundaries", *J. Comput. Phys*. Vol. **39**, pp. 201-225 (1981).

22. S. Osher and J. A. Sethian, "Fronts propagating with curvature-dependent speed: Algorithms based on Hamilton-Jacobi formulations", *J. Comput. Phys.* Vol. **79**, pp. 12-49 (1988).
23. M. Sussman, P. Smereka and S. Osher, "A Level Set Approach for Computing Solutions to Incompressible Two-Phase Flow", *J. Comput. Phys.* Vol. **114**, pp. 146-159 (1994).
24. J. A. Sethian, "Level Set Methods: Evolving Interfaces in Geometry, Fluid Mechanics, Computer Vision and Material Sciences", *Cambridge University Press, Cambridge, UK,* (1996).
25. D. L. Youngs, "An Interface Tracking Method for a 3D Eulerian Hydrodynamics Code", *Technical Report 44/92/35,* AWRE (1984).
26. W. J. Rider and D. B. Kothe, "Reconstructing Volume Tracking", *J. Comput. Phys.* Vol. **141**, pp. 112-152 (1998).
27. N. Ashgriz and J. Y. Poo, "FLAIR: Flux line-segment model for advection and interface reconstruction", *J. Comput. Phys.* Vol. **93**, pp.449-468 (1991).
28. M. Rudman, "Volume-Tracking Methods for Interfacial Flow Calculations", *Int. J. Numer. Methods Fluids.* Vol. **24**, pp. 671-691 (1997).
29. B. Lafaurie, C. Nardone, R. Scardovelli, S. Zaleski and G. Zanetti, "Modelling Merging and Fragmentation in Multiphase Flows with SURFER", *J. Comput. Phys.* Vol. **113**, pp. 134-147 (1994).
30. O. Ubbink, "Numerical predictions of Two Fluid Systems with Sharp Interfaces", *Ph.D. thesis, Department of Mechanical Engineering, Imperial College, University of London* (1997).
31. B. P. Leonard, "The ULTIMATE conservative difference scheme applied to unsteady one-dimensional advection", *Comput. Methods Appl. Mech. Engrg.* Vol. **88**, pp. 17-74 (1991).
32. M. S. Darwish, "A new high resolution scheme based on the normalised variable formulation", *Numer. Heat Transfer Part B.* Vol. **24**, pp. 353-371 (1993).
33. K. A. Pericleous & K. S. Chan, "The sea method for free surface problems with heat transfer and change of phase". In *Proc. Numerical Methods in Multiphase Flows,* 1994 ASME Fluids Engineering Division Summer Meeting, Lake Tahoe, Nevada, June 19-23, edited by C. T. Crowe *et al.* (1994).
34. B. P. Leonard, A. P. Lock and M. K. MacVean, "Conservative Explicit Unrestricted-Time-Step Multidimensional Constancy-Preserving Advection Schemes", *Monthly Weather Rev.* Vol. **124**, pp. 2588-2606 (1996).
35. O. Ubbink and R. I. Issa, "A Method for Capturing Sharp Fluid Interfaces on Arbitrary Meshes", *J. Comput. Phys.* Vol. **153**, pp. 26-50 (1999).
36. J. U. Brackbill, D. B. Kothe and C. Zemach, "A Continuum Method for Modelling Surface Tension", *J. Comput. Phys.* Vol. **100**, pp. 335-354 (1992).
37. S. V. Patankar and D. B. Spalding, "A Calculation Procedure for Heat, Mass and Momentum Transfer in three-dimensional Parabolic Flows", *Int. J. Heat Mass Transfer.* Vol. **15**, pp. 1787-1806 (1972).
38. M. Rhie and W. L. Chow, "A numerical study of the turbulent flow past an isolated airfoil with trailing edge separation", *AIAA J.* Vol **21**, pp. 1525-1532 (1983).
39. P. H. Gaskell and A. K. C. Lau, "Curvature-compensated convective-transport - SMART, A new boundedness-preserving transport algorithm", *Int. J. Numer. Methods Fluids* Vol. **8**, pp.617-641 (1988).
40. B. P. Leonard, "A stable and accurate convective modelling procedure based on quadratic upstream interpolation", *Comput Methods Appl. Mech. Engrg.* Vol. **19**, pp. 59-98 (1979).
41. S. T. Zalesak, "Fully Multidimensional Flux-Corrected Transport Algorithms for Fluids", *J. Comput. Phys.* Vol. **31**, pp. 335-362 (1979).
42. J. C. Martin and W. J. Moyce, "An Experimental Study of the Collapse of Liquid Columns on a Rigid Horizontal Plane", *Philosophical Transactions of the Royal Society of London. Series A, Mathematical and Physical Sciences.* Vol. **244**, pp. 312-324 (1952).

43.J. López, J. Hernández, P. Gómez and F. Faura, “An improved PLIC-VOF method for tracking thin fluid structures in incompressible two-phase flows”, *J. Comput. Phys.* Vol. **208**, pp. 51-74 (2005).

Council for the Central Laboratory of the Research Councils
Chilton, Didcot, Oxfordshire OX11 0QX, UK
Tel: +44 (0)1235 445000 Fax: +44 (0)1235 445808

CCLRC Rutherford Appleton Laboratory
Chilton, Didcot,
Oxfordshire OX11 0QX
UK
Tel: +44 (0)1235 445000
Fax: +44 (0)1235 44580

CCLRC Daresbury Laboratory
Keckwick Lane
Daresbury, Warrington
Cheshire WA4 4AD
UK
Tel: +44 (0)1925 603000
Fax: +44 (0)1925 603100

CCLRC Chilbolton Observatory
Drove Road
Chilbolton, Stockbridge
Hampshire SO20 6BJ
UK
Tel: +44 (0)1264 860391
Fax: +44 (0)1264 860142